Remote Sensing of Environment 221 (2019) 108–121

Contents lists available at ScienceDirect

Remote Sensing of Environment

journal homepage: www.elsevier.com/locate/rse

A disturbance weighting analysis model (DWAM) for mapping wildfire burn severity in the presence of forest disease

Yinan He[a], Gang Chen[a,*], Angela De Santis[b], Dar A. Roberts[c], Yuyu Zhou[d], Ross K. Meentemeyer[e,f]

[a] Laboratory for Remote Sensing and Environmental Change (LRSEC), Department of Geography and Earth Sciences, University of North Carolina at Charlotte, USA
[b] HOPE-Humanitarian Operations Foundation, Belgium
[c] Department of Geography, University of California, Santa Barbara, USA
[d] Department of Geological & Atmospheric Sciences, Iowa State University, USA
[e] Center for Geospatial Analytics, North Carolina State University, USA
[f] Department of Forestry and Environmental Resources, North Carolina State University, USA

ARTICLE INFO

Keywords:
Burn severity
Disturbance Weighting Analysis Model (DWAM)
Forestry
MESMA
Landsat
AVIRIS
Sudden oak death
Landscape epidemiology

ABSTRACT

Forest ecosystems are subject to recurring fires as one of their most significant disturbances. Accurate mapping of burn severity is crucial for post-fire land management and vegetation regeneration monitoring. Remote-sensing-based monitoring of burn severity faces new challenges when forests experience both fire and non-fire disturbances, which may change the biophysical and biochemical properties of trees in similar ways. In this study, we develop a Disturbance Weighting Analysis Model (DWAM) for accurately mapping burn severity in a forest landscape that is jointly affected by wildfire and an emerging infectious disease – sudden oak death. Our approach treats burn severity in each basic mapping unit (e.g., 30 m grid from a post-fire Landsat image) as a linear combination of burn severity of trees affected (diseased) and not affected by the disease (healthy), weighted by their areal fractions in the unit. DWAM is calibrated using two types of inputs: i) look-up tables (LUTs) linking burn severity and post-fire spectra for diseased and healthy trees, derived from field observations, hyperspectral sensors [e.g., Airborne Visible InfraRed Imaging Spectrometer (AVIRIS)], and radiative transfer models; and ii) pre-fire fractional maps of diseased and healthy trees, derived by decomposing a pre-fire Landsat image using Multiple Endmember Spectral Mixture Analysis (MESMA). Considering the presence of tree disease in DWAM improved the overall map accuracy by 42%. The superior performance is consistent across all three stages of disease progression. Our approach demonstrates the potential for improved mapping of forest burn severity by reducing the confounding effects of other biotic disturbances.

1. Introduction

Forest fires directly transform living and dead organic matter to charred or blackened residues in the short term (Kokaly et al., 2007; Lewis et al., 2007) and over the long term they affect the structure, function, and spatial patterns of ecological succession (Turner et al., 1998; Metz et al., 2013; Chen et al., 2015b). Building accurate knowledge of the spatial distribution of fire extent and particularly *burn severity* is crucial in planning and executing post-fire land management activities (Keeley, 2009; Quintano et al., 2017). Over the past decade, the term burn severity has gained popularity to represent the degree of environmental change (typically the loss of organic matter on the soil surface) caused by a fire (Key and Benson, 2006; Keeley, 2009). Both short-term (e.g., about within one year following the fire) and long-term (e.g. up to ten years) impacts of fire on local environment have been assessed to understand the direct loss of vegetation by combustion and longer term recovery, respectively (Key and Benson, 2005; Lentile et al., 2006; Roy et al., 2006). To date, there have been numerous studies about burn severity estimation across forest biomes worldwide (e.g., Díaz-Delgado and Pons, 2001; French et al., 2008; Hall et al., 2008; Miller et al., 2009). Due to rapid environmental change and intensive human interventions, burn severity mapping is increasingly challenged by compound disturbances in forest ecosystems; with increasing frequency forest landscapes are being impacted by emerging infectious diseases or other forms of disturbance prior to fire occurrence (Bright et al., 2013; Hultquist et al., 2014; van Mantgem et al., 2013). Because pre-fire disturbances also cause the loss of organic matter, estimating burn severity may introduce high uncertainties without properly considering the compound effects of multiple disturbances (Chen et al., 2017).

* Corresponding author.
E-mail address: gang.chen@uncc.edu (G. Chen).

https://doi.org/10.1016/j.rse.2018.11.015
Received 23 February 2018; Received in revised form 10 October 2018; Accepted 10 November 2018

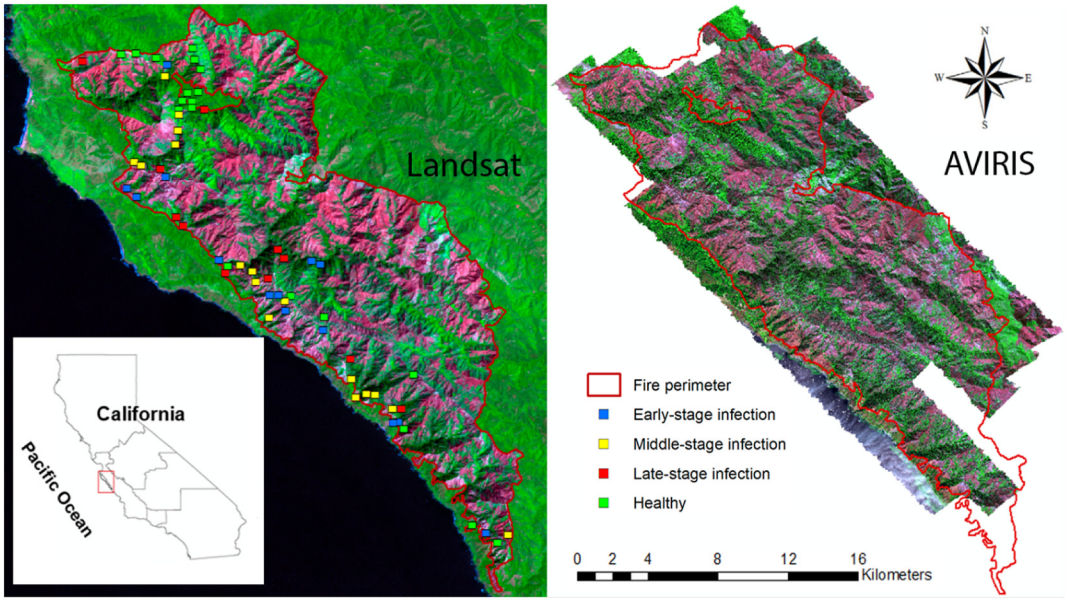

Fig. 1. Study area located in the Big Sur ecoregion on the western flank of the Santa Lucia Mountains in California. The Airborne Visible InfraRed Imaging Spectrometer (AVIRIS) image is from a colour composite using bands 195 (red), 52 (green) and 31 (blue). The Landsat TM image is from a colour composite using bands 7 (red), 4 (green) and 3 (blue). (For interpretation of the references to colour in this figure legend, the reader is referred to the web version of this article.)

Remote sensing is effective to assess fire effects on forest ecosystems at local, regional and continental scales (e.g., Chen et al., 2018; Hudak and Brockett, 2004; Lentile et al., 2006; Quintano et al., 2013; Veraverbeke et al., 2012). It is especially suitable for monitoring large and topographically complex landscapes that are logistically unfeasible with traditional field surveys (Chuvieco et al., 2007; Chen et al., 2015a). Remote sensing models to estimate burn severity are typically categorized into two groups: empirical and physical models. Specifically, classic empirical models rely on statistical regression (e.g., linear regression) or machine learning (e.g., random forests) to link sample field measurements of burn severity with remotely sensed data, e.g., spectral bands and indices (band combinations), such as Normalized Burn Ratio (NBR; López-García and Caselles, 1991), differenced Normalized Burn Ratio (dNBR; Key and Benson, 2006), and relative differenced Normalized Burn Ratio (RdNBR; Miller and Thode, 2007). Such models are relatively easy to implement and interpret. However, their performance depends highly on the reliability and sufficiency of field samples and is site-specific, which reduce their generality across complex geographic conditions (De Santis and Chuvieco, 2007). More recently, researchers took advantage of spectral mixing analysis to retrieve forest burn severity at the sub-pixel level from medium- or coarse-resolution, and even high-resolution imagery. For instance, the classic Multiple Endmember Spectral Mixing Analysis (MESMA; Roberts et al., 1998) has been used to derive non-photosynthetic vegetation fraction (NPV) or char fractions, which serve as an explanatory factor to estimate burn effects in forests (e.g., Fernandez-Manso et al., 2016; Meng et al., 2017; Quintano et al., 2017). While the spectra used in MESMA are typically from image sampling, they can also come from a radiative transfer model, as was true in Painter et al. (1998, 2003) and Sonnentag et al. (2007). Physical models attempt to address such limitation by simulating the physical interactions between radiation and burned canopies. A typical example is the use of radiative transfer models. Chuvieco et al. (2006) were the first to apply radiative transfer models, i.e., PROSPECT (Jacquemoud and Baret, 1990) and Kuusk (Kuusk, 2001) reflectance models, for burn severity estimation. De Santis et al. (2009) successfully simulated the spectra of burned canopies at 30 m resolution by integrating the leaf-level PROSPECT with the canopy-level GeoSail (Verhoef and Bach, 2003) models.

Despite the popularity of remote-sensing-based burn severity estimation, none of the present models explicitly account for the effects of pre-fire disturbances on map performance. Because both fire and non-fire disturbances (i.e., compound disturbances) may change the biophysical or biochemical properties of trees in similar ways (e.g., damaging tree structure or reducing foliage water content; Hultquist et al., 2014), pre- and post-fire spectral differences for the trees affected by non-fire disturbances are possibly different from their healthy counterparts. Uncertainties are further introduced if such non-fire disturbances affect forests at multiple stages showing various symptoms, leading to a weak relationship between spectral reflectance and burn severity. The negative impact of forest disease on burn severity estimation was recently confirmed by Chen et al. (2017), who employed PROSPECT and GeoSail to map burn severity in a forest that had been affected by an emerging infectious disease – sudden oak death – prior to fire occurrence. Their results revealed a significant overestimation of burn effects by ignoring tree damage caused by the disease.

The main goal of this study is to develop a remote-sensing-based model to map burn severity in forest landscapes, aiming to reduce the effects of tree damage caused by pre-fire disturbances. Here, we used sudden oak death as an example of a pre-fire disturbance that has caused widespread tree mortality in the Big Sur, California ecoregion before the studied Basin Complex Fire occurred in 2008 (Chen et al., 2015a). In model development, it is assumed that the final burn effect for a basic mapping unit (e.g., 30 m grid) is a linear combination of burn severity of two tree classes (i.e., trees affected and not affected by the disease), weighted by their areal fractions. To achieve the research goal, we also asked two specific questions in model development and assessment: (i) whether (and if yes, how much) the estimation of forest burn severity can be improved by incorporating pre-fire, disease-caused tree mortality? And (ii) how differently does the new model perform at the early, middle, and late stage of disease progression?

2. Study area

Our study site (centered at 36°16′ N, 121°44′ W) is located in the Big Sur ecoregion on the western flank of Santa Lucia Mountain of California with a total area of 28,383 ha (Fig. 1). The area has a Mediterranean-type climate and a rugged landscape dissected by steep slopes and drainages with elevations ranging from sea level to 1571 m

within 5 km of the coast (Meentemeyer et al., 2008). The area is dominated by a range of tree species: (i) mixed coniferous forest, composing of ponderosa pine (*Pinus ponderosa*), sugar pine (*Pinus lambertiana*), Jeffrey pine (*Pinus jeffreyii*), coulter pine (*Pinus coulteri*), and Santa Lucia fir (*Abies bracteata*), which are located on upper elevation slopes and rocky ridges; and (ii) mixed oak woodland consisting of coast live oak (*Quercus agrifolia*), Shreve's oak (*Q. parvula*), bay laurel (*Umbellularia californica*), and madrone (*Arbutus menziesii*), which were found on moister slopes, giving way to riparian corridors of redwood-tanoak forest at lower elevations. Since the mid-1990s, an invasive pathogen *Phytophthora ramorum* causing the disease – sudden oak death – has led to extensive tree mortality in the study area mainly found in two plant communities – mixed oak and redwood-tanoak forests (Rizzo et al., 2005). The disease involves a multi-year progress especially under a suitable temperature and rainfall conditions, girdling a tree over years or making the tree more susceptible to attack by other pathogens or insects (Chen et al., 2015b). In 2008, a wildfire – the Basin Complex Fire – was ignited by a dry lightning storm in late June and burned over 65,942 ha of federal, state and private lands. The total cost of containment action was around $77.2 million mainly due to the sheer size of the fires, the ruggedness of the terrain and the extremely dry conditions (USDA Forest Service, 2008). The Basin Complex Fire affected forest landscapes, which had and had not been damaged by sudden oak death.

3. Data and pre-processing

3.1. Field data

A solid network of long-term sudden oak death monitoring plots (500 m^2 each) in Big Sur was established in years 2006 and 2007 to understand the responses of forest communities (e.g., host mortality) to the invasion of sudden oak death (Meentemeyer et al., 2008). The plots were distributed in a stratified-random manner among two dominant tree types-redwood and mixed-evergreen within the study area. A Panasonic SXBlue real-time differential GPS (Geneq, Montreal) was applied for collecting plot positions, with an average accuracy of 1 m or less. A total of 61 plots were revisited after the wildfire in September and October 2008. Among these plots, 42 had been affected by sudden oak death, and 19 had not. The affected plots evenly covered the three stages of disease progression from early, middle, to late stages.

Burn severity at the plot level was recorded using the Composite Burn Index (CBI; Key and Benson, 2005) for five forest strata: (1) substrate layer, measured as changes to coarse woody debris, soil, duff, and leaf litter; (2) herb layer, changes or responses of vegetation < 1 m; (3) shrub layer, changes in vegetation higher than 1 m but < 5 m; (4) intermediate-sized tree layer, any trees higher than 5 m but standing under the dominant trees; and (5) dominant tree layer (Metz et al., 2011). In this study, all the CBI values were converted to geometrically structured CBI (GeoCBI) values (maximum: 2.83, minimum: 0.56, average: 2.00, and standard deviation: 0.42). Proposed by De Santis and Chuvieco (2009), GeoCBI (ranging from 0.0–3.0) simulates burn severity with a 'top-down' view, to be consistent with remote sensing observations. GeoCBI accounts for the contribution of each forest stratum using its Fraction Cover (FCOV) as the weighting factor (see Eq. (1)).

$$\text{GeoCBI} = \frac{\sum_{m_1}^{m_n} (CBI_m * FCOV_m)}{\sum_{m_1}^{m_n} FCOV_m} \quad (1)$$

where *FCOV* is calculated and characterized as the percentage of vegetation coverage with respect to the total size of the plot area, *m* is the identification of each stratum, and *n* is the number of strata.

3.2. AVIRIS imagery

The AVIRIS image mosaic (from seven transects) at the 3 m resolution was acquired on September 24, 2008, immediately following the containment of the Basin Complex Fire for rapid assessment. AVIRIS is an imaging spectrometer that measures 224 contiguous spectral bands in the range of ~360 nm to ~2500 nm with an average bandwidth of 10 nm (Green et al., 1998). The images were geometrically corrected, radiometrically calibrated, and were made available at the JPL's website (http://aviris.jpl.nasa.gov). Atmospheric correction was performed using the Fast Line-of-sight Atmospheric Analysis of Spectral Hypercubes (FLAASH) module, which is available in the ENVI software package (ITT Visual Information Solutions, Colorado, USA). FLAASH uses the physics-based radiative transfer model MODTRAN 5 to perform atmospheric correction, which needs flight and sensor metadata (i.e., sensor type, scene center latitude/longitude, average ground elevation, sensor altitude, and flight date and time), as well as assumed or measured atmospheric parameters (i.e., atmosphere model, aerosol model, and atmosphere water vapor) to generate apparent surface reflectance spectra from radiance data (Berk et al., 2006). In our study, flight and sensor metadata are available with the image. To simulate atmospheric conditions, Mid-Latitude Summer (MLS) was selected as an atmosphere model (Matthew et al., 2002), as AVIRIS data were acquired in September (temperature around 210 °C) at the latitude 36°N. Also because our study area is not strongly affected by urban or industrial sources, the rural aerosol model was selected (Shettle and Fenn, 1979). In order to compute apparent surface reflectance using radiative transfer equations in MODTRAN 5, the column water vapor amount for each pixel was determined using the 1135 nm water vapor absorption feature (Kruse, 2004). To mitigate topographic effects as the study area is a mountainous region, a Terrain Agular Bin method (TAB; Wen et al., 2014) was applied to correct for topographic effects using a 30 m resolution digital elevation model (DEM) derived from the data collected by Advanced Spaceborne Thermal Emission and Reflection Radiometer (ASTER) as part of the Global Digital Elevation Model Version 2 (GDEM V2) project (ASTER GDEM Validation Team, 2011).

3.3. Landsat imagery

Two cloud-free Landsat-5 Thematic Mapper (TM) scenes (path 43, row 35) were acquired on May 13, 2008, and September 2, 2008, from the USGS Landsat Surface Reflectance High-Level Data Products (Schmidt et al., 2013) to represent pre- and post-fire forest conditions in the study area. The images have solar zenith angles of 26.6° and 36.2°, and solar azimuth angles of 124.7° and 135.9°, respectively. The data were downloaded via the U.S. Geological Survey Landsat data portal and had been geometrically, radiometrically, and topographically corrected before being made available online. In this study, we used six TM bands (1–5, and 7).

4. Methods

Our Disturbance Weighting Analysis Model (DWAM) includes three major steps (Fig. 2): (i) development of GeoCBI-spectrum look-up tables (LUTs), (ii) pre-fire fractional mapping, and (iii) burn severity mapping. To facilitate the succeeding model description and discussion, we defined the trees not affected by sudden oak death as '*healthy trees*', and those affected as '*diseased trees*', regardless of the burn effects. The overall methodological flow is briefly described in this paragraph. In step (i), we developed two LUTs linking burn severity as measured by GeoCBI with spectra for healthy and diseased trees, respectively. To do so, we used two spectral libraries: one was developed by De Santis and Chuvieco (2009), and the other one was derived from the post-fire AVIRIS data. In step (ii), we mapped fractional cover of healthy and diseased trees prior to fire occurrence, which was completed by applying the spectral unmixing MESMA model to the pre-fire Landsat TM

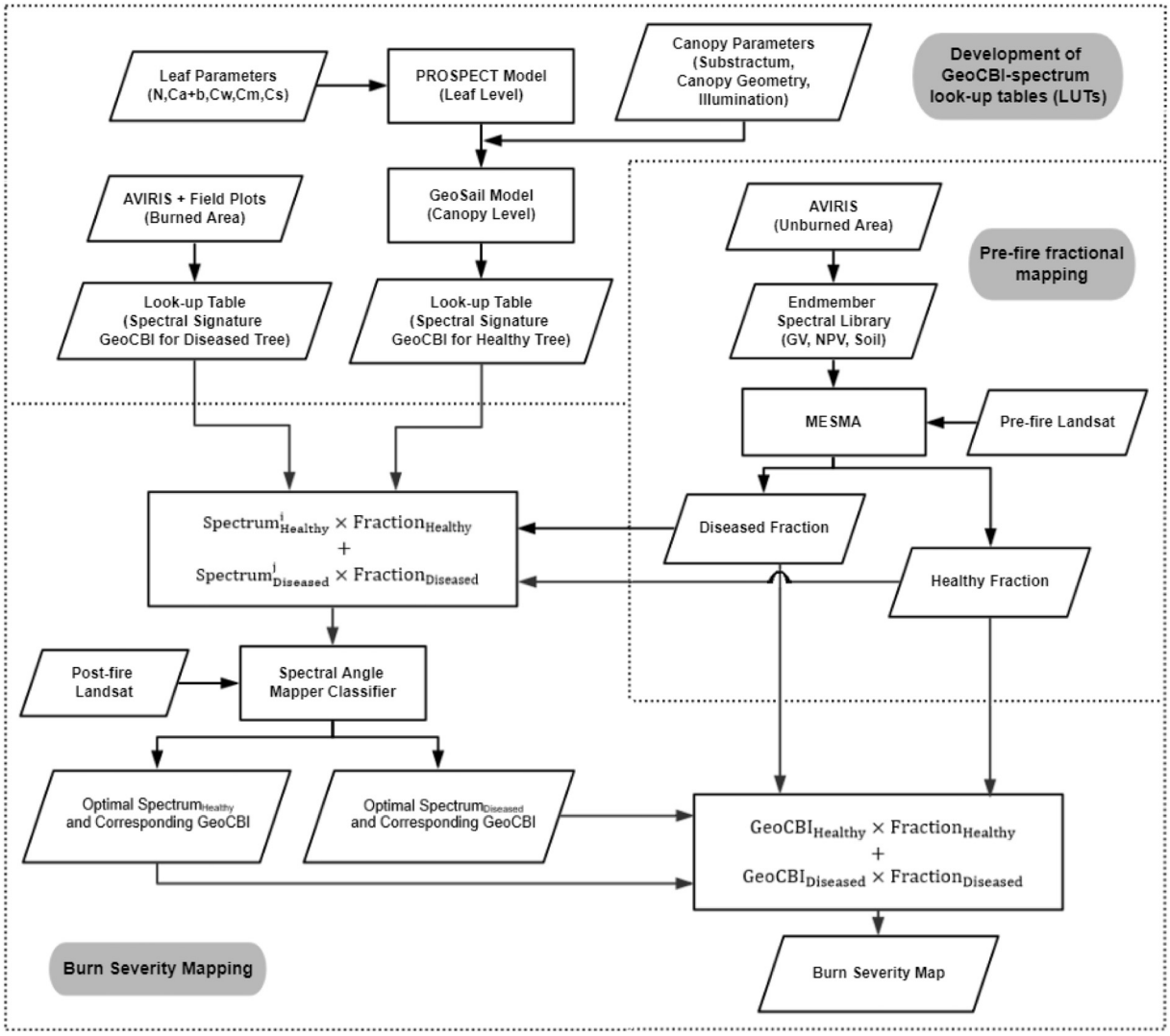

Fig. 2. Methodological workflow used in this study.

image. The AVIRIS data acquired outside of the fire scar was used to construct a spectral library consisting of healthy trees, diseased trees, and soil. In step (iii), we estimated burn severity (in 30 m grids) as a linear combination of burn severity of healthy and diseased trees, weighted by their areal fractions in each grid.

Finally, we evaluated DWAM performance using field-measured GeoCBI data. In order to further understand the effects of disease progression on DWAM performance, we mapped disease infection at the early, middle, and late stages, and analyzed the relationship between infection stages and model performance. For the purpose of comparison, we also assessed burn severity with the traditional spectral-index-based approach, e.g., NBR, dNBR and RdNBR, which used both pre- and post-fire imagery.

4.1. Development of GeoCBI-spectrum LUTs

4.1.1. LUT for healthy trees

A spectral library for healthy trees was derived from a research project by De Santis and Chuvieco (2009), who studied forest burn severity in the Mediterranean ecosystem, where our study area is also located. Here, we did not use data from our study mainly due to the fact that only 11 healthy plots were covered by the AVIRIS image, preventing the extraction of meaningful LUT relating spectra and GeoCBI. The spectral library was developed using two radiative transfer models PROSPECT (Jacquemoud and Baret, 1990) and GeoSail (Verhoef and Bach, 2003) in two steps: (i) at the leaf level, the PROSPECT model was used to simulate spectra for brown (damaged by fire) and green (undamaged) leaves, where the input values included leaf structural parameter, chlorophyll a + b, equivalent water thickness, dry matter content, and brown pigments content (De Santis et al., 2009). (ii) The output of the PROSPECT model, together with a series of canopy parameters (substratum type, geometry, and illumination) (De Santis et al., 2009), was used as inputs for parameterizing the GeoSail model, scaling up the spectral library from the leaf to the canopy level. A LUT was built to link 30 reference spectra with burn severity GeoCBI values from 0 to 3 (De Santis et al., 2009). To facilitate the application of the LUT to Landsat TM bands, each of the spectra in the LUT was convolved to the Landsat spectral resolution, using a Gaussian model with a full width at half maximum (FWHM) appropriate for the TM band spacing (Mutanga et al., 2015).

4.1.2. LUT for diseased trees

We built a LUT for diseased trees by taking advantage of the AVIRIS data acquired in our study area (see Section 3.3). We overlaid field-measured plots on the AVIRIS image and extracted GeoCBI values from the plots and the corresponding spectra from the image. This information was used to create a LUT linking 39 spectra with 39 GeoCBI values in diseased forests. Among a total of 42 plots identified to be

affected by sudden oak death in the field (Section 3.2), three plots were removed because they were not covered by the AVIRIS image. Subsequently, the spectra in the LUT were convolved to the Landsat TM spectral resolution following the same method as described in Section 4.1.1.

4.2. Pre-fire fractional mapping

4.2.1. Spectral library

We constructed a spectral library for pre-fire fractional mapping. Here, we applied AVIRIS data to identify endmembers for green vegetation (GV) and non-photosynthetic vegetation (NPV), representing healthy and diseased trees, respectively. Because the AVIRIS sensor was flown after fire occurrence, endmember extraction was conducted in the areas outside the fire scar. Specifically, we applied the Pixel Purity Index (PPI; Boardman et al., 1995) algorithm to identify a pool of potential endmember pixels in the AVIRIS image. PPI is an iterative process, in which every pixel is repeatedly projected onto a random vector selected through the n-dimensional scatter plot (n = 224 in our study), and pixels are considered pure if they consistently fall into the tails of the calculated histograms. After the initial assessment, the number of endmembers was further reduced using the three techniques proposed by Roberts et al. (2003), Dennison and Roberts (2003), and Dennison et al. (2004): Count based Endmember Selection (CoB), Endmember Average RMSE (EAR), and Minimum Average Spectral Angle (MASA). To do so, we selected the endmembers that modeled the greatest number of endmembers within their classes using CoB. When EAR was considered, we chose endmembers that yielded the lowest RMSE within each class. In addition, we identified the endmembers with the lowest average spectral angle when MASA was taken into account. The final endmembers were selected to satisfy all of the three criteria: highest COB, lowest EAR and lowest MASA. Using the Visualization and Image Processing for Environmental Research (VIPER) Tools package (Roberts et al., 2007), we developed a spectral library, including 6 spectra for GV, 5 spectra for NPV, 6 spectra for soil, and 1 spectrum for shade. Finally, all the AVIRIS spectra were convolved to the Landsat TM spectral resolution.

4.2.2. Fractional mapping

Using the endmember spectral library and the MESMA model, we decomposed each pixel in the pre-fire Landsat image into GV (healthy tree), NPV (diseased tree), soil, and shade fractions. The parameters for calibrating MESMA included minimum and maximum allowable fraction values for each class, maximum shade fraction, and RMSE. In this project, we chose −0.05 and 1.05 for minimum and maximum allowable fraction values, respectively, 0.8 for maximum allowable shade fraction value, and 0.025 for maximum allowable RMSE, following the recommendations by Dennison and Roberts (2003). Here, the minimum and maximum possible values were allowed to be slightly < 0 or slightly > 1, because the precision of sub-pixel fraction estimation is typically limited by the Modular Transfer Function (MTF) of Landsat sensor; and the spectral signal for a given pixel is partially influenced by the land cover of surrounding pixels (Forster, 1985; Townshend et al., 2000). While multiple models met the above-mentioned criteria, the model with the lowest RMSE was selected. Then, the MESMA derived three types of fractional (GV, NPV, and soil) maps. Finally, three relative abundance images of non-shade endmembers with values ranging from 0 to 1 were obtained. We employed VIPER to complete the MESMA procedures (Roberts et al., 2007).

4.3. Burn severity mapping

Burn severity mapping was carried out using the post-fire Landsat TM image based on an assumption that burn severity in each pixel (covered by a mixture of healthy and diseased trees) is a linear combination of burn severity for two tree classes – healthy and diseased trees, weighted by their areal fractions. To determine the burn severity value for each class, it is also assumed that the spectral reflectance of each burned pixel is the linear combination of reflectance spectra of burned canopies from healthy and diseased trees, weighted by their areal fractions (Eq. (2)).

$$Reflectance_{i,j} = Spectrum^{i}_{\text{Healthy}} \times F_{\text{Healthy}} + Spectrum^{j}_{\text{Diseased}} \times F_{\text{Diseased}} \quad (2)$$

where $spectrum_{\text{Healthy}}{}^{i}$ represents the ith spectrum (range: 1 to 30) from the reference spectra in the healthy tree LUT (Section 4.1.1), F_{Healthy} is the pre-fire fraction of healthy trees in the pixel area (Section 4.2), $spectrum_{\text{Diseased}}{}^{j}$ represents the jth spectrum (range: 1 to 39) from the reference spectra in the diseased tree LUT (Section 4.1.2), and F_{Diseased} is the pre-fire fraction of diseased trees in the pixel area (Section 4.2).

To determine the two optimal spectra (one for healthy trees and one for diseased trees), we evaluated all 1170 spectral combinations (30 × 39). Each of the calculated reflectance spectra from Eq. (2) was compared with the reflectance of the corresponding Landsat pixel (at the same location) using the Spectral Angle Mapper algorithm (SAM; Kruse et al., 1993). Here, SAM measures the similarity (i.e., angle) between the calculated and the observed spectral reflectance across Landsat TM bands. SAM has proven effective in forest burn severity assessment due to its simplicity and insensitivity to differences in illumination (De Santis et al., 2009). The optimal spectra were chosen when the simulated reflectance reached the highest similarity with the observed reflectance, among all the tested spectral combinations. Consequently, the corresponding GeoCBI values were derived from the two LUTs. The estimated burn severity for each pixel area is the linear combination of burn severity of healthy and diseased trees, weighted by their areal fractions (Eq. (3)). This is based on an assumption that the actual burn severity from a burned plot should be aggregated using the same proportions of healthy and diseased trees.

$$Burn\ severity = GeoCBI_{\text{Healthy}} \times F_{\text{Healthy}} + GeoCBI_{\text{Diseased}} \times F_{\text{Diseased}} \quad (3)$$

where $GeoCBI_{\text{Healthy}}$ represents burn severity of healthy trees, $GeoCBI_{\text{Diseased}}$ represents burn severity of diseased trees, F_{Healthy} is the fraction of healthy trees within each pixel, and F_{Diseased} is the fraction of diseased trees within each pixel.

For model calibration and validation, Leave-One-Out-Cross-Validation (LOOCV) was applied due to the limited number of field-measured diseased plots (39 plots). Specifically, for each round of evaluation, one observation was left out for model performance evaluation (computing RMSE), while the remainder was used for building the diseased tree LUT.

4.4. Infection stage mapping

Depending on the invasion stages of sudden oak death, an infected forest landscape may show three major symptoms (Meentemeyer et al., 2008; Chen et al., 2015a): (i) early-stage (host trees retaining their dried foliage and fine twigs for one year or more), (ii) middle-stage (some older mortality with host trees losing fine crown fuels and surface fuels beginning to accumulate for 1–3 years), and (iii) late-stage (host trees being dead for over 4 years and causing gaps due to trees falling over). To understand the infection stages in the studied forest landscape at the time of fire occurrence, we employed the sudden oak death-caused tree mortality maps from a previous project (He et al., under review). In that project, MESMA was used to extract NPV fractions from Landsat TM annual time series. The results were refined using Species Distribution Modeling (SDM) that simulated the statistical probability of sudden oak death dispersal patterns over space and time, leading to annual map accuracies from 74.24% to 82.50%. In our study, we referenced the annual disease maps and divided the diseased trees into three infection stages following three criteria: (1) all of the trees that had been killed in or prior to 2005 were identified as the late stage;

(2) the infection that occurred in 2006 and 2007 was identified as the middle stage; and (3) the newly detected infection in 2008 was identified as the early stage. The mapping result was validated using field-measured data, with overall accuracy, producer's accuracy, user's accuracy, and kappa statistic reported in this study.

4.5. Burn severity assessment with NBR, dNBR and RdNBR

For the purpose of comparison, we calculated popular remote sensing spectral indices (i.e., NBR, dNBR and RdNBR) for burn severity estimation. Particularly, dNBR and RdNBR take into consideration the pre- and post-fire spectral reflectance, which are also used in DWAM. To do so, we applied the following equations to calculate these indices (López-García and Caselles, 1991; Key and Benson, 2006; Miller and Thode, 2007).

$$NBR = \frac{B_4 - B_7}{B_4 + B_7} \quad (4)$$

$$dNBR = NBR_{Pre-fire} - NBR_{Post-fire} \quad (5)$$

$$RdNBR = \frac{NBR_{Pre-fire} - NBR_{Post-fire}}{\sqrt{ABS(NBR_{Pre-fire}/1000)}} \quad (6)$$

where B_4 and B_7 are the spectral reflectance of band 4 (near infrared, NIR) and band 7 (short wave infrared, SWIR) of Landsat TM, respectively. Then, we developed linear regression models linking individual spectral indices with GeoCBI, with R^2 and RMSE reported.

5. Results

5.1. Spectral libraries

The average spectral reflectance for burned trees (a – healthy; b – diseased) is presented in Fig. 3. We also divided burn severity into five main intervals, i.e., GeoCBI ∈ [0, 1.0), [1.0, 1.5), [1.5, 2.0), [2.0, 2.5], and (2.5, 3.0]. In most cases, the reflectance curves show similar patterns for both diseased and healthy trees (Fig. 3), where wildfire reduces forest spectral reflectance with the increase of burn severity from the visible to the near-infrared portion of the spectrum. However, burn severity leads to a higher variation of spectral reflectance in healthy trees than in diseased trees, particularly when GeoCBI values are larger than 1.0 (Fig. 3). In the shortwave infrared portion of the spectrum, the patterns are different. For diseased trees, varying levels of burn severity result in noticeable differences in reflectance curves. However, for healthy trees, the spectral reflectance corresponding to two medium-high burn severity intervals (GeoCBI ∈ [1.5, 2.0), [2.0, 2.5]) show similar reflectance. In the same shortwave infrared portion, we further found a stronger effect of medium-low burn severity [GeoCBI ∈ [1.0, 1.5)] on diseased trees than healthy trees, resulting in lower spectral reflectance.

To facilitate calculating pre-fire fractions for healthy and diseased trees, we extracted 6 GV, 5 NPV, and 6 soil endmembers (see methods in Section 4.2.1), with their spectra shown in Fig. 4. We found a high intra-class spectral variability among GV endmembers, possibly due to the high variety of tree species types (e.g., mixed oak woodlands and mixed coniferous forests) in the study area. In contrast, the spectral signatures from disease-affected trees (i.e., NPV reflectance) and soil are relatively homogeneous.

5.2. Fraction maps

The shade normalized fraction maps corresponding to the three endmembers – GV, NPV, and soil are illustrated in Fig. 5, where light colors represent high fractions and dark colors show low fractions. High values in the NPV fraction map mainly distribute along the west coast, which is consistent with the findings by Chen et al. (2017), who used one-meter resolution KOMPSAT-2 satellite data to map sudden oak death-caused tree mortality over the same area. However, a small portion of high-value pixels were observed to spread all over the region, suggesting an overestimation of disease occurrence by only using NPV as the proxy of disease-caused tree mortality.

5.3. Burn severity maps

We generated two types of burn severity maps. For the first one, we assumed that all the trees were in the similar, healthy conditions prior to fire occurrence (i.e., the fractions of disease-affected trees were assigned value '0' in DWAM). For the second one, we considered the disease effects using the proposed model DWAM. For simplicity purposes, the resulting burn severity maps were named as non-DWAM map (not considering disease) and DWAM map (considering disease). Both maps are dominated by moderate (1.5 ≤ GeoCBI < 2.5) to severe burns (2.5 ≤ GeoCBI ≤ 3.0). While severe burns dominate the non-DWAM map with a spatial coverage of 78.9% (Fig. 6a), they only account for 27.3% in the DWAM map (Fig. 6b), in which moderate burns dominate (66.6%).

We further compared field-measured and estimated GeoCBI values using two scatter plots in Fig. 7. Similar to the findings as illustrated in Fig. 6, ignoring the effects of disease on burn severity modeling caused an evident overestimation with a relatively large error (RMSE = 0.62; Fig. 7a). Using the proposed model, we were able to reduce the error (RMSE) to 0.36, a 42% decrease (Fig. 7b). We also found that the proposed DWAM can reduce the overestimation of burn severity in both moderately and severely burned plots (Fig. 6).

Table 1 provides summary statistics (area, percentage, minimum, maximum, mean, median and standard deviation) of the estimated burn

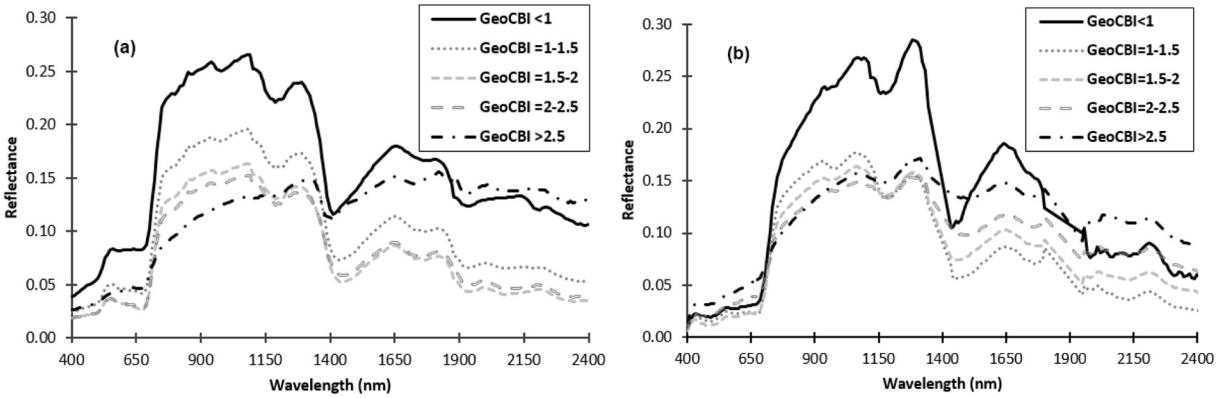

Fig. 3. Average spectral reflectance corresponding to the main intervals of GeoCBI for (a) healthy and (b) diseased trees. Healthy tree spectra were derived from De Santis and Chuvieco (2009).

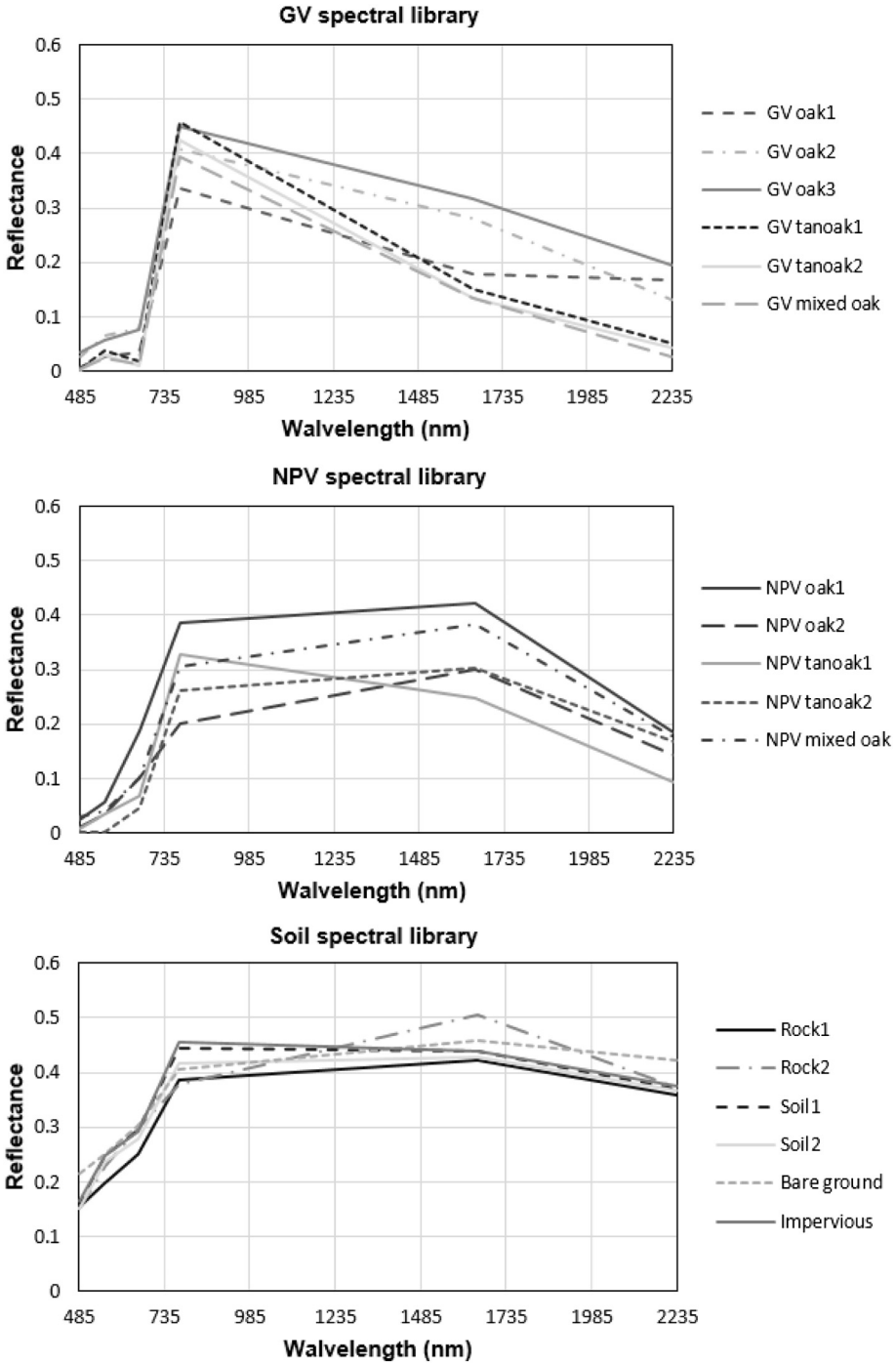

Fig. 4. The extracted endmember spectra for green vegetation (GV), non-photosynthetic vegetation (NPV), and soil. (For interpretation of the references to colour in this figure legend, the reader is referred to the web version of this article.)

severity at three levels (low, moderate and high) using non-DWAM and DWAM. Overall, DWAM considers that the majority of the area was subject to moderate burn severity, while the area is considered to be heavily burned with non-DWAM.

5.4. Infection stage map

The overall accuracy of mapping the stages of sudden oak death infection is 69.84%, with a Kappa coefficient of 0.58 (Fig. 8). As presented in Table 2, the producer's accuracies of diseased forest across the three progression stages are high (early-stage: 81.81%, middle-stage: 81.25%, late-stage: 85.71%), while the corresponding user's accuracies are relatively lower (early-stage: 64.28%, middle-stage: 76.47%, late-stage: 54.54%). This indicates a slight overestimation of disease infection. Trees may have been affected by both sudden oak death and other disturbances (e.g., drought and strong wind). Especially at the late stage, tree gaps may be filled with trunks, branches, leaves and/or low-level, live vegetation (e.g., shrubs). The symptom of infestation was not as apparent as that at the early-middle stages (see a review by Chen and Meentemeyer, 2016), increasing uncertainties in disease mapping. Although the disease progression map contains errors, it did not affect burn severity modeling in our study and serves as valuable baseline data for assessing the performance of our model across stages of disease progression.

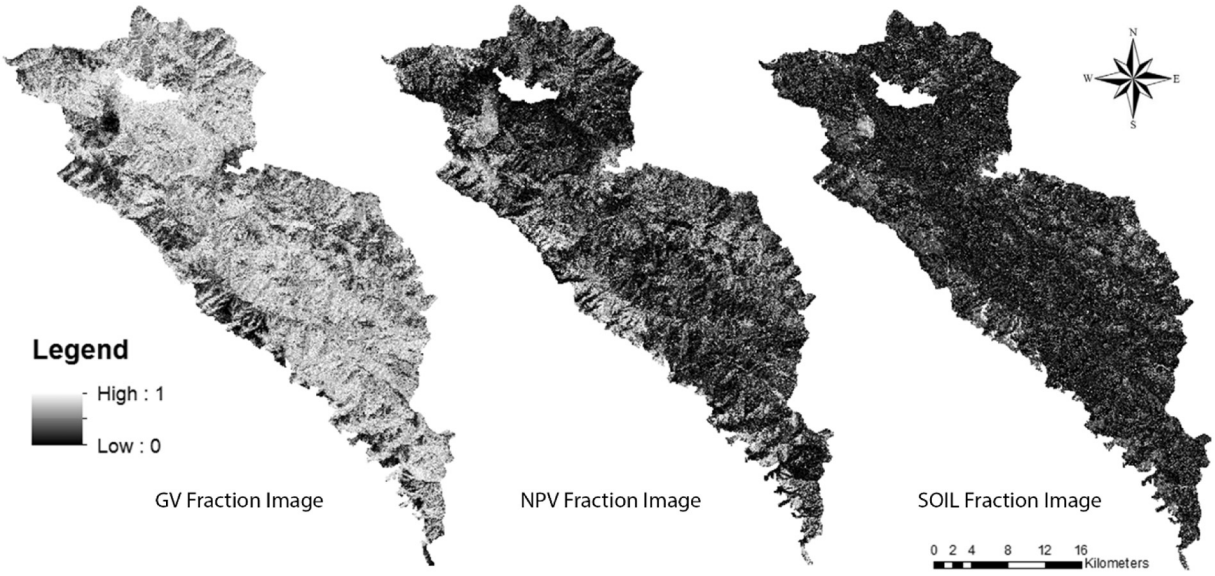

Fig. 5. Fraction maps of green vegetation (GV), non-photosynthetic vegetation (NPV), and soil derived from the pre-fire Landsat image, where values range from low (black tone) to high (light tone). (For interpretation of the references to colour in this figure legend, the reader is referred to the web version of this article.)

5.5. Performance of NBR, dNBR and RdNBR

We compared field-measured GeoCBI values with those estimated by NBR, dNBR, and RdNBR using scatter plots in Fig. 9. In most cases (except the middle-stage infestation), dNBR and RdNBR that account for the spectral difference between pre- and post-fire conditions reveal better fitting performance and smaller errors than NBR that uses only post-fire data across stages of disease progression. The performance of dNBR and RdNBR are comparable. While dNBR shows a better agreement (higher R^2 and smaller RMSE) with GeoCBI at the early stage of infestation, RdNBR offers a relatively better solution in burn severity estimation at the middle and late stages (Fig. 9).

6. Discussion

6.1. Assessment of burn severity mapping

The evaluation of DWAM and non-DWAM maps (Fig. 7) suggests an overestimation of burn severity if pre-fire disease disturbances are not considered in modeling. In fact, the comparison between the two maps is equivalent to the comparison between our model and the physical simulation model proposed by De Santis et al. (2009). This is because when disease fractions are treated as zeros, DWAM only relies on the spectral library and LUT developed for healthy trees, using the same inputs and procedure as those in De Santis's radiative transfer modeling framework (De Santis et al., 2009). Their framework has proven effective in areas that did not contain intensive disease disturbances (e.g., De Santis et al., 2010). However, in our study site, the high spectral

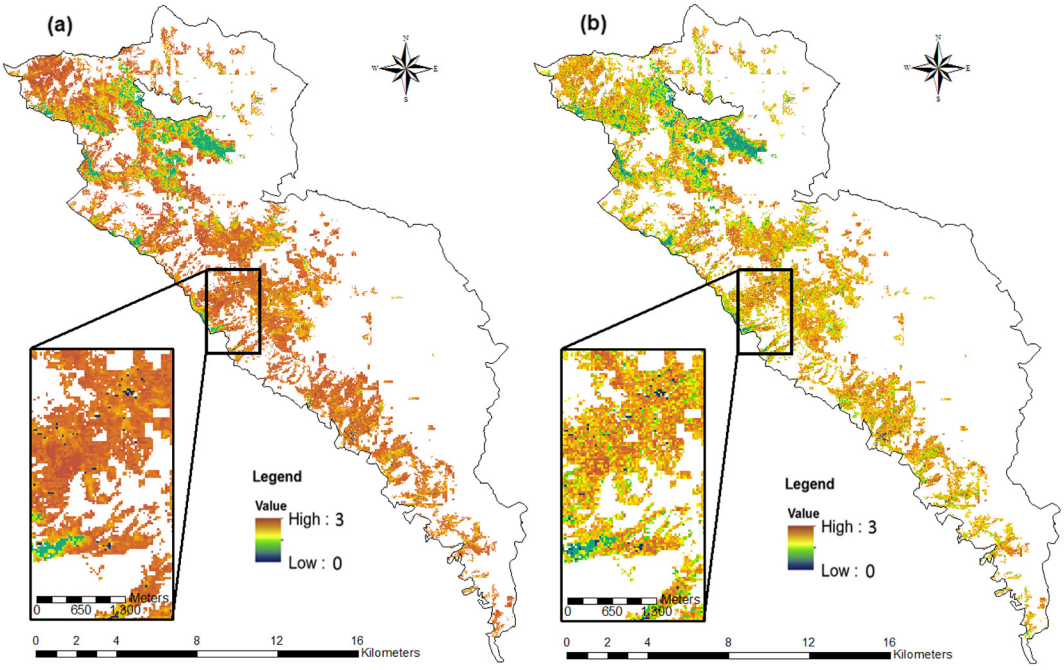

Fig. 6. Burn severity maps (a) without considering the effects of sudden oak death, and (b) considering the disease effects using DWAM.

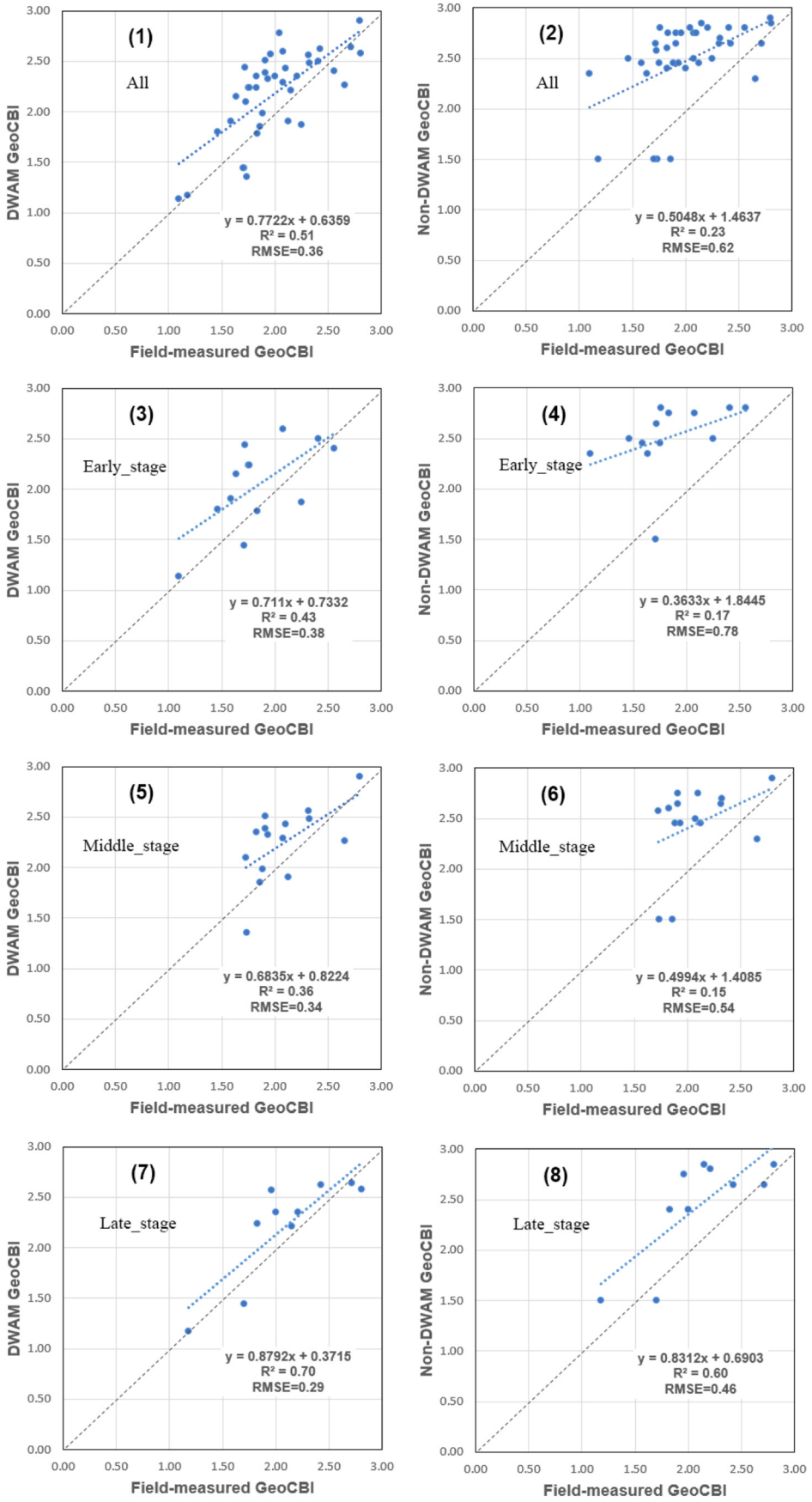

Fig. 7. Comparisons between field-measured and estimated GeoCBI (2,4,6,8) without considering the effects of sudden oak death, and (1,3,5,7) considering the disease effects using DWAM across all the infected plots, and the plots at the early-, middle-, and late-stage infection, respectively.

Table 1
Summary statistics of the estimated burn severity using non-DWAM and DWAM.

Burn severity		Area (ha)	Percentage (%)	Minimum	Maximum	Mean	Median	Standard deviation
Non-DWAM	Low	60.5	0.7	0.00	1.00	0.74	1.00	0.33
	Moderate	1720.8	20.4	1.50	2.45	2.07	2.30	0.39
	High	6691.5	78.9	2.50	3.00	2.71	2.75	0.11
DWAM	Low	509.6	6.1	0.00	1.49	1.31	1.40	0.23
	Moderate	5627.7	66.6	1.50	2.49	2.21	2.27	0.22
	High	2314.1	27.3	2.50	2.99	2.62	2.60	0.09

similarity between diseased and burned tree patches (Hultquist et al., 2014) can possibly confuse the development of one single, accurate LUT linking burn severity and spectra, because a portion of diseased trees (burned or not) may be treated as being affected (or more severely affected) by fire. This is evidenced in Table 1, where the non-DWAM map contains 78.9% of severe burns (GeoCBI ∈ [2.5, 3.0]); but the same level of burn severity only accounts for 27.3% in the DWAM map that has a higher estimation accuracy. Further because forest landscapes typically show various symptoms corresponding to different stages of disease progression (Meentemeyer et al., 2008), the relationship between spectra and burn severity becomes complicated as such relationship may vary from one disease-affected area to another. It is therefore meaningful and effective, as demonstrated in our study, to develop separate spectral libraries and LUTs for healthy and diseased trees in burn severity estimation.

Spectral mixture analysis (SMA) has been recently introduced in burn severity estimation (e.g., Veraverbeke et al., 2014; Quintano et al., 2017). So far, the main strategy is decomposing post-fire optical imagery (typically using MESMA) to extract NPV or char fractions at the sub-pixel level, which are statistically linked to burn severity. Although

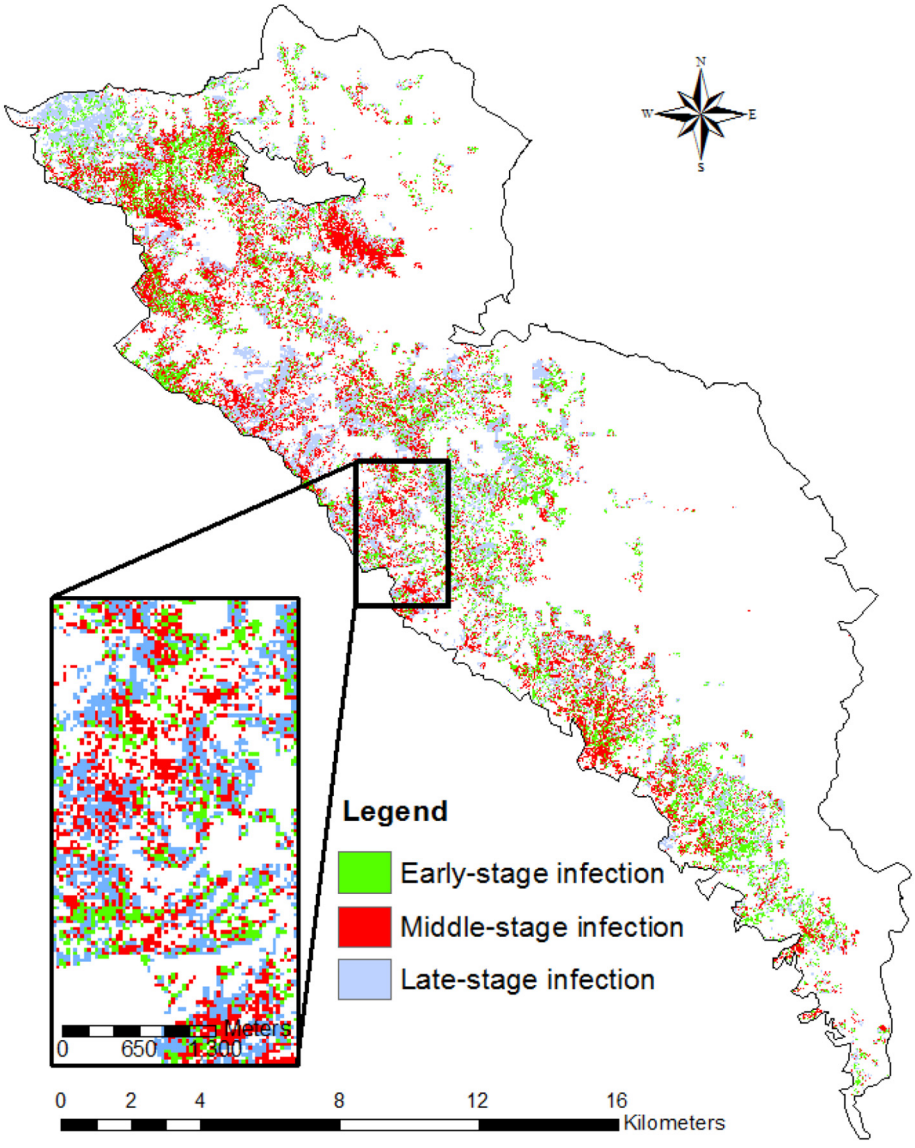

Fig. 8. Forest disease infection map showing early-, middle-, and late-stage disease progression.

Table 2
Confusion matrix for the infection stage mapping result.

User class	Reference class					
	Healthy forest	Early-stage	Middle-stage	Late-stage	Total	Producer's accuracy (%)
Healthy forest	16	5	3	3	27	59.25
Early-stage	2	9	0	0	11	81.81
Middle-stage	1	0	13	2	16	81.25
Late-stage	0	0	1	6	7	85.71
Total	19	14	17	11	61	
User's accuracy (%)	84.21	64.28	76.47	54.54		

Overall accuracy = 69.84%; Kappa statistic = 0.58.

DWAM also utilizes SMA and MESMA, our model differs from the others by incorporating fractions of two broad tree classes (diseased and healthy trees) from pre-fire imagery. The fractions are used to identify the optimal spectrum for each of the two tree classes, and consequently, burn severity is estimated using the GeoCBI-spectrum LUTs. While this strategy is not as straightforward as directly extracting NPV or char fractions (e.g., Quintano et al., 2017), we circumvent the challenge of potentially obtaining large errors in post-fire image decomposition, because the disturbed trees by sudden oak death and fire demonstrate similarities in spectral reflectance (Hultquist et al., 2014).

Our model takes advantage of both pre- and post-fire Landsat imagery to quantify disease effects. This strategy is similar to several empirical approaches in the way that differentiates pre- and post-fire spectral indices, e.g., dNBR (Key and Benson, 2006) and RdNBR (Miller and Thode, 2007). While these spectral indices are able to capture the spectral variation caused by pre-fire disturbances, it becomes problematic to establish a robust statistical relationship between burn severity and the extracted spectral differences. For trees not affected by sudden oak death, the difference between pre- and post-fire spectral reflectance has been found to be positively correlated with burn severity, although such relationship may not significant in diseased tree patches (Chen et al., 2015b). Based on the calculation of dNBR and RdNBR in this study, we found that DWAM explained 51% of the variance in all the data, while each of the dNBR- and RdNBR-based models explained 29% (Fig. 7 versus Fig. 9). It is also true for the three stages of disease progression, suggesting that DWAM can better capitalize on the pre- and post-fire imagery to fit the data than using the spectral-index-based approach in our study area. As Metz et al. (2011) and Chen et al. (2017) pointed out, sudden oak death-caused increases in surface fuels may reduce a tree's resistance to fire and in turn lead to high burn severity. This suggests that with the occurrence of sudden oak death, the pre- and post-fire spectral differences for diseased trees are possibly smaller than those of their healthy counterparts, possibly underestimating burn severity (Fig. 9). Uncertainties are further introduced by various symptoms of tree mortality corresponding to multiple stages of infection, leading to a weak statistical relationship between spectral indices and burn severity. This is particularly true for the early or middle stage of infestation, where the pre- and post-fire spectral similarity is higher than that at the late stage. Finally, the spectral-index-based approach is empirically-based, which typically requires new field data for model training at a new site or human interventions for determining the thresholds of burn severity classes (Eidenshink et al., 2007). Field data in our model are mainly used for developing GeoCBI-spectrum LUTs. Our model has the potential to be directly used in an area having similar tree species types and disturbances, i.e., similar LUTs, as ours. However, the spectral-index-based approach is more mature and has been widely used at regional to national scales, such as the United States' MTBS (Monitoring Trends in Burn Severity) program (https://www.mtbs.gov). Thorough evaluations on DWAM are expected before our model is applicable to large areas.

6.2. Performance of burn severity mapping across stages of disease progression

The results from DWAM and non-DWAM maps were both found to be stage-dependent (Tables 3 and 4). Compared to the other two stages, the late stage contains more trees that suffered from severe burns (Table 3). Despite the errors in mapping stages of sudden oak death infection, at all stages, the non-DWAM map shows a consistent bias with the highest proportion of severely burned landscape (80.9% for the early stage, 72% for the middle stage, and 87.4% for the late stage; Table 3). In contrast, DWAM can reduce the overestimation of burn severity at all the three stages, resulting in a landscape dominated by moderate burns (Table 4). Particularly at the early and middle stages, a large portion of the study area, which is considered as highly burned in the non-DWAM map, is dominated by moderate burns in the DWAM map. This suggests that DWAM is more likely to show a superior performance in the areas where trees still retain fine twigs and large branches, i.e., trees were recently affected by the disease. This is in an agreement with our field experience and can be explained by the fact that diseased trees were mistreated as burned trees as a result of similar changes in biophysical or biochemical properties. Overall, forest responses to disturbances at various stages (e.g., disease progression) can introduce different levels of uncertainties in remote assessment of burn severity. Better understanding the spectrum-disturbance relationship, such as constructing a stage-based spectral library, may further improve the performance of burn severity mapping. However, such type of effort also leads to increased workloads and high costs in data acquisition.

7. Conclusions

Forest ecosystems are facing a variety of disturbances including fires and emerging infectious diseases. Especially when both fire and non-fire disturbances coexist, high uncertainties are introduced to the remote assessment of burn severity. In this study, we developed a new model DWAM to accurately estimate burn severity by incorporating the effects of pre-fire, disease-caused tree mortality. Our burn severity estimation has an average error of 0.36, a 42% improvement as compared to the result without consideration of disease effects. We have further compared DWAM with popular spectral-index-based approaches using dNBR and RdNBR for the purpose of assessing the generalization capacity of DWAM. Our model's improvements were observed at all three stages of disease progression. While being developed at one study site, DWAM demonstrates several strengths making it potentially suitable for burn severity mapping in other regions. First, we have carefully selected a California study area for model development. The site features a representative Mediterranean climate and has been widely studied for forest disturbances, including disease and fire. Second, the model was developed to study the general fire-disease effect. The assumptions, input data and three model components are not tied to local environment of specific requirements. Third, DWAM has the potential to be calibrated in areas affected by another type of disease/insect disturbance, e.g., mountain pine beetle (Assal et al., 2014). The structure of DWAM remains the same. Field observations, hyperspectral imagery, and/or radiative transfer models can be used to build spectral libraries and LUTs for capturing the relationship between post-fire spectra and burn severity. However, we also note that the generalization potential of DWAM needs to be thoroughly evaluated at independent sites to ensure that the model is applicable to large-scale burn severity mapping.

Acknowledgements

This research was supported by the National Science Foundation (EF-0622770) as part of the joint NSF-NIH Ecology and Evolution of

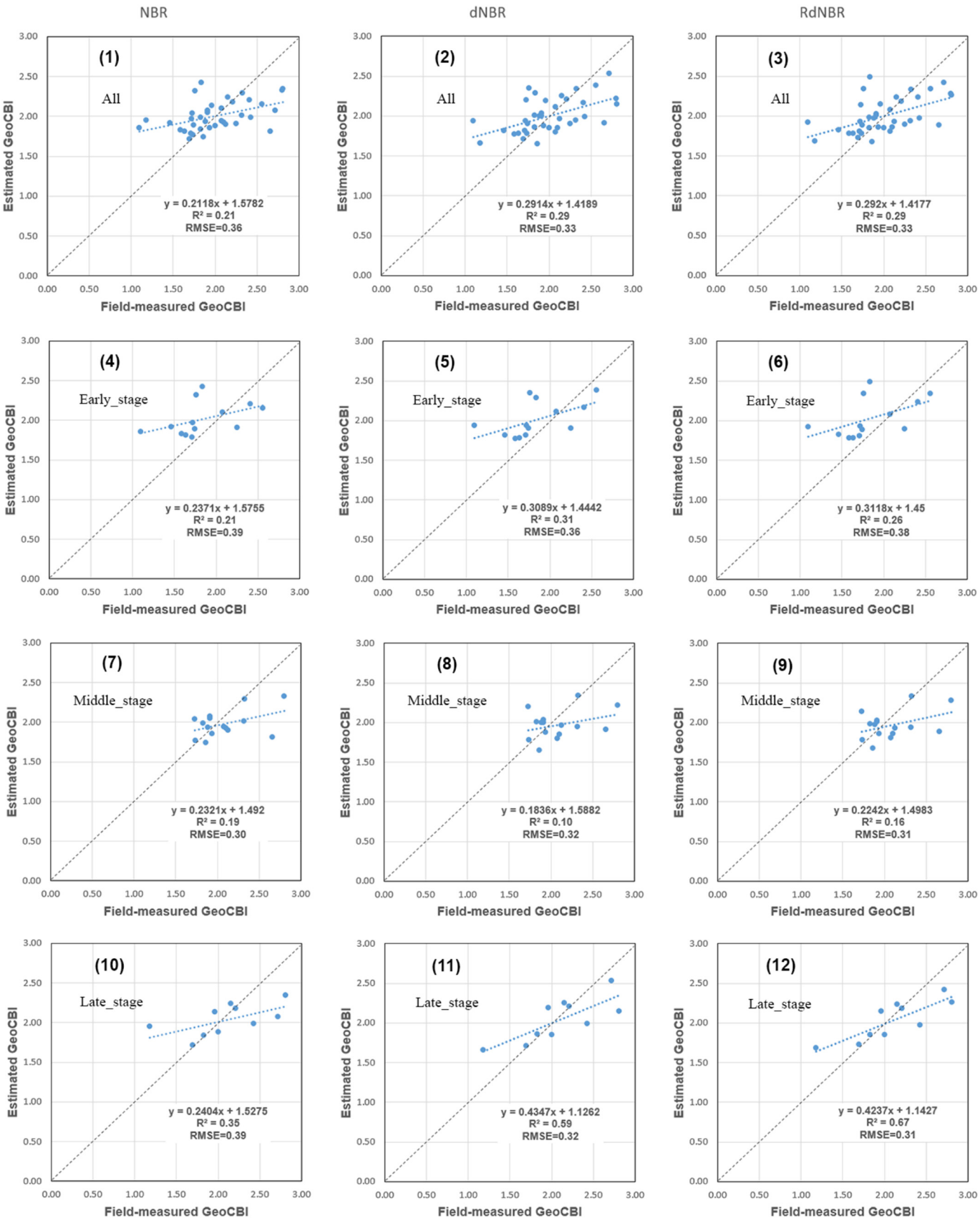

Fig. 9. Comparisons between field-measured GeoCBI and NBR-, dNBR-, RdNBR-based GeoCBI across all the disease infected plots, and the plots at the early-, middle-, and late-stage infection, respectively.

Table 3
Summary statistics of the burn severity in forests across three types of forests: early-, middle-, and late-stage disease progression in the non-DWAM map.

Burn severity non-DWAM		Area (ha)	Percentage (%)	Minimum	Maximum	Mean	Median	Standard deviation
Early stage	Low	16.8	1.1	0.00	1.00	0.71	1.00	0.34
	Moderate	279.7	18.0	1.50	2.45	2.11	2.30	0.38
	High	1256.5	80.9	2.50	3.00	2.70	2.70	0.10
Middle stage	Low	15.3	0.7	0.00	1.00	0.75	1.00	0.32
	Moderate	588.3	27.3	1.50	2.45	1.97	2.0	0.41
	High	1552.5	72.0	2.50	3.00	2.71	2.75	0.11
Late stage	Low	5.6	0.3	0.00	1.00	0.61	0.50	0.37
	Moderate	256.4	12.3	1.50	2.45	2.04	2.20	0.39
	High	1820.5	87.4	2.50	3.00	2.76	2.80	0.10

Table 4
Summary statistics of the burn severity in forests across three types of forests: early-, middle-, and late-stage disease progression in the DWAM map.

Burn severity DWAM		Area (ha)	Percentage (%)	Minimum	Maximum	Mean	Median	Standard deviation
Early stage	Low	84.3	5.4	0.00	1.49	1.25	0.39	0.29
	Moderate	1056.4	68.0	1.50	2.49	2.23	2.28	0.21
	High	412.9	26.6	2.50	3.00	2.60	2.58	0.08
Middle stage	Low	231.1	10.7	0.00	1.49	0.34	1.40	0.18
	Moderate	1408.3	65.3	1.50	2.49	2.19	2.25	0.23
	High	517.5	24.0	2.50	3.00	2.62	2.60	0.09
Late stage	Low	82.0	3.9	0.00	1.49	1.34	1.42	0.22
	Moderate	1232.1	59.2	1.50	2.49	2.22	2.27	0.21
	High	768.0	36.9	2.50	3.00	2.63	2.62	0.09

Infectious Disease program, the North Carolina Space Grant, and the University of North Carolina at Charlotte CLAS Junior Faculty Development Award. The authors also gratefully acknowledge financial support from the USDA Forest Service – Pacific Southwest Research Station, the Gordon and Betty Moore Foundation. We thank numerous contributors who provided vital field and laboratory support, including K. Aram, M. Beh, A. Brauer, M. Chan, R. Cobb, C, DeLong, W. Dillon, K. Frangioso, J. Geng, A. Hohl, H. Mehl, A. Oguchi, E. Paddock, K. Pietrzak, M. Vaclavikova, J. Vieregge, L. Waks and A. Wickland.

References

Assal, T.J., Sibold, J., Reich, R., 2014. Modeling a Historical Mountain pine beetle outbreak using Landsat MSS and multiple lines of evidence. Remote Sens. Environ. 155, 275–288.

ASTER GDEM Validation Team, 2011. ASTER Global Digital Elevation Model Version 2 – Summary of Validation Results. Available online at. http://www.jspacesystems.or.jp/ersdac/GDEM/ver2Validation/Summary_GDEM2_validation_report_final.pdf.

Berk, A., Anderson, G.P., Acharya, P.K., Bernstein, L.S., Muratov, L., Lee, J., Fox, M., Adler-Golden, S.M., Chetwynd Jr., J.H., Hoke, M.L., Lockwood, R.B., Gardner, J.A., Cooley, T.W., Borel, C.C., Lewis, P.E., Shettle, E.P., 2006. MODTRAN5: 2006 Update. Proceedings of SPIE - The International Society for Optical Engineering, pp. 62331F.

Boardman, J.W., Kruse, F.A., Green, R.O., 1995. Mapping target signatures via partial unmixing of AVIRIS data. In: Summaries, Fifth JPL Airborne Earth Science Workshop. Jet Propulsion Laboratory, Pasadena, CA, pp. 23–26.

Bright, B.C., Hicke, J.A., Meddens, A.J.H., 2013. Effects of bark beetle-caused tree mortality on biogeochemical and biogeophysical MODIS products. J. Geophys. Res. Biogeosci. 118, 974–982.

Chen, G., Meentemeyer, R.K., 2016. Remote sensing of forest damage by diseases and insects. In: Weng, Q. (Ed.), Remote Sensing for Sustainability. CRC Press, Taylor & Francis Group, Boca Raton, Florida, pp. 145–162.

Chen, G., Metz, M.R., Rizzo, D.M., Dillon, W.W., Meentemeyer, R.K., 2015a. Object-based assessment of burn severity in diseased forests using high-spatial and high-spectral resolution MASTER airborne imagery. ISPRS J. Photogramm. Remote Sens. 102, 38–47.

Chen, G., Metz, M.R., Rizzo, D.M., Meentemeyer, R.K., 2015b. Mapping burn severity in a disease-impacted forest landscape using Landsat and MASTER imagery. Int. J. Appl. Earth Obs. Geoinf. 40, 91–99.

Chen, G., He, Y., De Santis, A., Li, G., Cobb, R., Meentemeyer, R.K., 2017. Assessing the impact of emerging forest disease on wildfire using Landsat and KOMPSAT-2 data. Remote Sens. Environ. 195, 218–229.

Chen, G., Weng, Q., Hay, G.J., He, Y., 2018. Geographic object-based image analysis (GEOBIA): emerging trends and future opportunities. GIScience Remote Sens. 55, 159–182.

Chuvieco, E., Riaño, D., Danson, F.M., Martin, P., 2006. Use of a radiative transfer model to simulate the postfire spectral response to burn severity. J. Geophys. Res. Biogeosci. 111 (G4), 1–15.

Chuvieco, E., De Santis, A., Riaño, D., Halligan, K., 2007. Simulation approaches for burn severity estimation using remotely sensed images. J. Assoc. Fire Ecol. 3, 129–150.

De Santis, A., Chuvieco, E., 2007. Burn severity estimation from remotely sensed data: performance of simulation versus empirical models. Remote Sens. Environ. 108, 422–435.

De Santis, A., Chuvieco, E., 2009. GeoCBI: a modified version of the composite burn index for the initial assessment of the short-term burn severity from remotely sensed data. Remote Sens. Environ. 113, 554–562.

De Santis, A., Chuvieco, E., Vaughan, P.J., 2009. Short-term assessment of burn severity using the inversion of PROSPECT and GeoSail models. Remote Sens. Environ. 113, 126–136.

De Santis, A., Asner, G.P., Vaughan, P.J., Knapp, D.E., 2010. Mapping burn severity and burning efficiency in California using simulation models and Landsat imagery. Remote Sens. Environ. 114, 1535–1545.

Dennison, P.E., Roberts, D.A., 2003. Endmember selection for multiple endmember spectral mixture analysis using endmember average RMSE. Remote Sens. Environ. 87, 123–135.

Dennison, P.E., Halligan, K.Q., Roberts, D.A., 2004. A comparison of error metrics and constraints for multiple endmember spectral mixture analysis and spectral angle mapper. Remote Sens. Environ. 93, 359–367.

Díaz-Delgado, R., Pons, X., 2001. Spatial patterns of forest fires in Catalonia (NE of Spain) along the period 1975–1995 analysis of vegetation recovery after fire. For. Ecol. Manag. 147, 67–74.

Eidenshink, J., Schwind, B., Brewer, K., Zhu, Z.-L., Quayle, B., Howard, S., 2007. A project for monitoring trends in burn severity. Fire Ecol. 3, 3–21.

Fernandez-Manso, A., Quintano, C., Roberts, D.A., 2016. Burn severity influence on post-fire vegetation cover resilience from Landsat MESMA fraction images time series in Mediterranean forest ecosystems. Remote Sens. Environ. 184, 112–123.

Forster, B., 1985. An examination of some problems and solutions in monitoring urban areas from satellite platforms. Int. J. Remote Sens. 6, 139–151.

French, N., Kasischke, E., Hall, R., Murphy, K., Verbyla, D., Hoy, E., Allen, J., 2008. Using Landsat data to assess fire and burn severity in the North American boreal forest region: an overview and summary of results. Int. J. Wildland Fire 17, 443–462.

Green, R.O., Eastwood, M.L., Sarture, C.M., Chrien, T.G., Aronsson, M., Chippendale, B.J., Faust, J.A., Pavri, B.E., Chovit, C.J., Solis, M.S., Olah, M.R., Williams, O., 1998. Imaging spectroscopy and the airborne visible infrared imaging spectrometer (AVIRIS). Remote Sens. Environ. 65, 227–248.

Hall, R.J., Freeburn, J.T., De Groot, W.J., Pritchard, J.M., Lynham, T.J., Landry, R., 2008. Remote sensing of burn severity: experience from western Canada boreal fires. Int. J. Wildland Fire 17, 476–489.

He, Y., Chen, G., Potter, C., Meentemeyer, R.K., 2018. Integrating multi-sensor remote sensing and species distribution modeling to map the spread of emerging forest disease and tree mortality. Remote Sens. Environ (under review).

Hudak, A.T., Brockett, B.H., 2004. Mapping fire scars in a southern African savannah using Landsat imagery. Int. J. Remote Sens. 25, 3231–3243.

Hultquist, C., Chen, G., Zhao, K., 2014. A comparison of Gaussian process regression, random forests and support vector regression for burn severity assessment in diseased forests. Remote Sens. Lett. 5, 723–732.

Jacquemoud, S., Baret, F., 1990. PROSPECT: a model of leaf optical properties spectra. Remote Sens. Environ. 34, 75–91.

Keeley, J.E., 2009. Fire intensity, fire severity and burn severity: a brief review and

suggested usage. Int. J. Wildland Fire 18, 116–126.
Key, C.H., Benson, N.C., 2005. Landscape assessment: ground measure of severity, the Composite Burn Index and remote sensing of severity, the Normalized Burn Ratio. In: Lutes, D.C., Keane, R.E., Caratti, J.F., Key, C.H., Benson, N.C., Gangi, L.J. (Eds.), FIREMON: Fire Effects Monitoring and Inventory System. USDA Forest Service, Rocky Mountain Research Station, Gen. Tech. Rep. RMRS-GTR-164pp. CD:LA1–LA51 Ogden, UT.
Key, C.H., Benson, N.C., 2006. Landscape assessment (LA) sampling and analysis methods. In: USDA Forest Service General Technical Report, RMRS-GTR-164-CD.
Kokaly, R.F., Rockwell, B.W., Haire, S.L., King, T.V.V., 2007. Characterization of post-fire surface cover, soils, and burn severity at the Cerro Grande Fire, New Mexico, using hyperspectral and multispectral remote sensing. Remote Sens. Environ. 106, 305–325.
Kruse, F.A., 2004. Comparison of ATREM, ACORN, and FLAASH atmospheric corrections using low-altitude AVIRIS data of boulder. In: CO. Jpl Airborne Geoscience Workshop.
Kruse, F.A., Lefkoff, A.B., Boardman, J.W., Heidebrecht, K.B., Shapiro, A.T., Barloon, P.J., Goetz, A.F.H., 1993. The spectral image processing system (SIPS)-interactive visualization and analysis of imaging spectrometer data. Remote Sens. Environ. 44, 145–163.
Kuusk, A., 2001. A two-layer canopy reflectance model. J. Quant. Spectrosc. Radiat. Transf. 71, 1–9.
Lentile, L.B., Holden, Z.A., Smith, A.M.S., Falkowski, M.J., Hudak, A.T., Morgan, P., Lewis, S.A., Gessler, P.E., Benson, N.C., 2006. Remote sensing techniques to assess active fire characteristics and post-fire effects. Int. J. Wildland Fire 15, 319–345.
Lewis, S., Lentile, L., Hudak, A., Robichaud, P., Morgan, P., Bobbitt, M., 2007. Mapping ground cover using hyperspectral remote sensing after the 2003 Simi and old wildfires in Southern California. Fire Ecol. 3, 109–128.
López-García, M.J., Caselles, V., 1991. Mapping burns and natural reforestation using thematic mapper data. Geocarto Int. (1), 31–37.
van Mantgem, P.J., Nesmith, J.C.B., Keifer, M., Knapp, E.E., Flint, A., Flint, L., 2013. Climatic stress increases forest fire severity across the western United States. Ecol. Lett. 16, 1151–1156.
Matthew, M.W., Adler-Golden, S.M., Berk, A., Felde, G., Anderson, G.P., Gorodetzky, D., Paswaters, S., Shippert, M., 2002. Atmospheric correction of spectral imagery: evaluation of the FLAASH algorithm with AVIRIS data. In: Proceedings of the 31st Applied Imagery Pattern Recognition Workshop, pp. 157–163.
Meentemeyer, R.K., Rank, N.E., Shoemaker, D.A., Oneal, C.B., Wickland, A.C., Frangioso, K.M., Rizzo, D.M., 2008. Impact of sudden oak death on tree mortality in the Big Sur ecoregion of California. Biol. Invasions 10, 1243–1255.
Meng, R., Wu, J., Schwager, K.L., Zhao, F., Dennison, P.E., Cook, B.D., Brewster, K., Green, T.M., Serbin, S.P., 2017. Using high spatial resolution satellite imagery to map forest burn severity across spatial scales in a pine barrens ecosystem. Remote Sens. Environ. 191, 95–109.
Metz, M.R., Frangioso, K.M., Meentemeyer, R.K., Rizzo, D.M., 2011. Interacting disturbances: wildfire severity affected by stage of forest disease invasion. Ecol. Appl. 21, 313–320.
Metz, M.R., Varner, J., Frangioso, K., 2013. Unexpected redwood mortality from synergies between wildfire and an emerging infectious disease. Ecology 94, 2152–2159.
Miller, J.D., Thode, A.E., 2007. Quantifying burn severity in a heterogeneous landscape with a relative version of the delta normalized burn ratio (dNBR). Remote Sens. Environ. 109, 66–80.
Miller, J.D., Safford, H.D., Crimmins, M., Thode, A.E., 2009. Quantitative evidence for increasing forest fire severity in the Sierra Nevada and southern Cascade Mountains, California and Nevada, USA. Ecosystems 12, 16–32.
Mutanga, O., Adam, E., Adjorlolo, C., Abdel-Rahman, E.M., 2015. Evaluating the robustness of models developed from field spectral data in predicting African grass foliar nitrogen concentration using Worldview-2 image as an independent test dataset. Int. J. Appl. Earth Obs. Geoinf. 34, 178–187.
Painter, T.H., Roberts, D.A., Green, R.O., Dozier, J., 1998. The effect of grain size on spectral mixture analysis of snow-covered area from AVIRIS data. Remote Sens. Environ. 65, 320–332.
Painter, T.H., Dozier, J., Roberts, D.A., Davis, R.E., Green, R.O., 2003. Retrieval of subpixel snow-covered area and grain size from imaging spectrometer data. Remote Sens. Environ. 85, 64–77.
Quintano, C., Fernández-Manso, A., Roberts, D.A., 2013. Multiple Endmember Spectral Mixture Analysis (MESMA) to map burn severity levels from Landsat images in Mediterranean countries. Remote Sens. Environ. 136, 76–88.
Quintano, C., Fernandez-Manso, A., Roberts, D.A., 2017. Burn severity mapping from Landsat MESMA fraction images and land surface temperature. Remote Sens. Environ. 190, 83–95.
Rizzo, D.M., Garbelotto, M., Hansen, E.M., 2005. *Phytophthora ramorum*: integrative research and management of an emerging pathogen in California and Oregon forests. Annu. Rev. Phytopathol. 43, 309–335.
Roberts, D.A., Gardner, M., Church, R., Ustin, S., Scheer, G., Green, R.O., 1998. Mapping chaparral in the Santa Monica Mountains using multiple endmember spectral mixture models. Remote Sens. Environ. 65, 267–279.
Roberts, D.A., Dennison, P.E., Gardner, M.E., Hetzel, Y., Ustin, S.L., Lee, C.T., 2003. Evaluation of the potential of Hyperion for fire danger assessment by comparison to the airborne visible/infrared imaging spectrometer. IEEE Trans. Geosci. Remote Sens. 41, 1297–1310.
Roberts, D.A., Halligan, K., Dennison, P., 2007. VIPER Tools User Manual. V1.5.
Roy, D.P., Boschetti, L., Trigg, S.N., 2006. Remote sensing of fire severity: assessing the performance of the normalized burn ratio. IEEE Geosci. Remote Sens. Lett. 3, 112–116.
Schmidt, G., Jenkerson, C., Masek, J., Vermote, E., Gao, F., 2013. Landsat ecosystem disturbance adaptive processing system (LEDAPS) algorithm description. In: U.S. Geological Survey Open-File Report 2013-1057. U.S. Geological Survey, Reston, VA, p. 27. U.S. Geological Survey, Reston, VA Available online. https://pubs.usgs.gov/of/2013/1057/.
Shettle, E.P., Fenn, R.W., 1979. Models for the Aerosols of the Lower Atmosphere and the Effects of Humidity Variations on their Optical Properties. Environmental Research Papers Air Force Geophys. Lab., Bedford, Mass, pp. 94.
Sonnentag, O., Chen, J.M., Roberts, D.A., Talbot, J., Halligan, K.Q., Govind, A., 2007. Mapping tree and shrub leaf area indices in an ombrotrophic peatland through multiple endmember spectral unmixing. Remote Sens. Environ. 109, 342–360.
Townshend, J.R.G., Huang, C., Kalluri, S.N.V., Defries, R.S., Liang, S., Yang, K., 2000. Beware of per-pixel characterization of land cover. Int. J. Remote Sens. 21, 839–843.
Turner, M.G., Baker, W.L., Peterson, C.J., Peet, R.K., 1998. Factors influencing succession: lessons from large, infrequent natural disturbances. Ecosystems 1, 511–523.
USDA Forest Service, 2008. Executive Summary: Basin Complex Fire/Indians Fire BAER Initial Assessment. pp. 16.
Veraverbeke, S., Hook, S., Hulley, G., 2012. An alternative spectral index for rapid fire severity assessments. Remote Sens. Environ. 123, 72–80.
Veraverbeke, S., Stavros, E.N., Hook, S.J., 2014. Assessing fire severity using imaging spectroscopy data from the Airborne Visible/Infrared Imaging Spectrometer (AVIRIS) and comparison with multispectral capabilities. Remote Sens. Environ. 154, 153–163.
Verhoef, W., Bach, H., 2003. Simulation of hyperspectral and directional radiance images using coupled biophysical and atmospheric radiative transfer models. Remote Sens. Environ. 87, 23–41.
Wen, J.G., Zhao, X.J., Liu, Q., Tang, Y., Dou, B.C., 2014. An improved land-surface albedo algorithm with DEM in rugged terrain. IEEE Geosci. Remote Sens. Lett. 11, 883–887.